SLAC-PUB-16892

3D Electron Tracking and Vertexing in Single Plane Pixel Detectors

G. Blaj*, *Member, IEEE*, C. J. Kenney, *Member, IEEE*, C. E. Chang, P. Caragiulo, A. Dragone, G. Haller, *Member, IEEE*, P. Hansson, C. Hast, R. Herbst, *Member, IEEE*, B. Markovic, T. Smith

***Abstract*—In particle physics, tracking and vertexing typically relies on silicon strip or pixel detectors arranged in multiple planes. The ePix100a detector was developed for low noise x-ray detection. When used for high energy particle tracking and imaging, it yields a signal to noise ratio (SNR) of 500 to 1000. The unusually large SNR allows accurate reconstruction of tracks, down to subpixel resolution and 3D angular information. This paper presents (1) results obtained at the End Station Test Beam (ESTB) facility at SLAC National Laboratory with 4.5 GeV beams, incident at several different angles, (2) an analytical approach to accurately reconstruct 3D track position and orientation using single plane detectors, and (3) measurements with scattering targets, demonstrating the performance of the approach presented here. The same approach can be used with any other highly energetic charged particle detection, allowing good 3D position and orientation measurements using fewer or even single silicon detector planes.**

***Keywords*—GeV electron detection, Tracking, Vertexing, Pixel detector, ePix, Silicon sensor.**

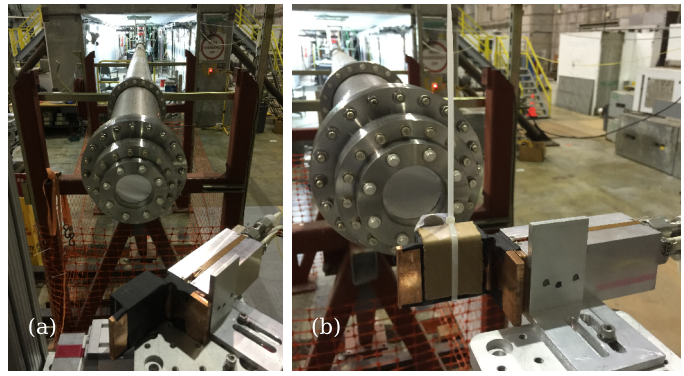

Fig. 1. End Station Test Beam (ESTB) facility at SLAC showing the End Station A beam pipe and an ePix100a detector: (a) at a $45°$ orientation with the beam, and (b) perpendicular to the beam, with a small scattering target (lead brick, $10\,\mathrm{mm}$ thick) attached with a cable tie to the front of the detector (approximately $10\,\mathrm{mm}$ from the sensor).

I. Introduction

In particle physics, tracking and vertexing relies strongly on silicon-based detectors, including strip detectors (noise $\sim 1000\,\mathrm{e}^-$ to $2000\,\mathrm{e}^-$), pixel detectors (noise $\sim 10\,\mathrm{e}^-$ to $100\,\mathrm{e}^-$), and others [1]. These detectors are typically arranged in multiple planes in order to allow accurate reconstruction of the vertices.

One of the earliest pixel detectors for measuring tracks of high energy particles could already resolve subpixel resolutions and partial 3D track orientations using single plane monolithic detectors [2]. More recent advances greatly increased the signal to noise ratio and allowed reduced pixel sizes, resulting in increased accuracy of 3D track reconstruction.

The ePix100A pixel detector was developed for low noise x-ray photon detection and imaging [3], [4]. In GeV electron detection, they allow imaging electron tracks in the Si sensor with a signal to noise ratio of ~ 500 to 1000. This unusually high SNR yields detailed information about the electron tracks, down to subpixel resolution and accurate 3D angle information.

In this paper we present results obtained at the End Station Test Beam (ESTB) [5] facility at SLAC National Laboratory with $4.5\,\mathrm{GeV}$ electron beams intersecting a single plane ePix100a detector at several different angles. Subsequently, we introduce an analytical approach to accurately reconstruct 3D track position and orientation using single plane detectors. Finally, we present measurements with a scattering target, demonstrating the performance of the virtual vertexing approach presented here.

II. Methods

A. Experimental Setup

The experiments described in this paper were performed at the End Station Test Beam (ESTB) facility [5] at SLAC National Accelerator Laboratory, Menlo Park, CA, U.S.A. This facility can use $5\,\mathrm{Hz}$ of the Linac Coherent Light Source (LCLS) [6] electron beam. ESTB is a unique high energy physics (HEP) resource, with a high-energy (up to $15\,\mathrm{GeV}$) primary electron beam with clean secondary electron beams for, e.g., detector development. Fig. 1 shows the end of the electron beam pipe. A parallel electron beam with an energy of $4.5\,\mathrm{GeV}$ was used.

For detection we used an ePix100a hybrid pixel detector [7]. This detector was initially designed for low-noise imaging of x-ray photons and is built on the ePix platform [8] of x-ray detectors. The main characteristics are summarized in Table I. The ePix100a ASIC is flip-chip-bonded onto a silicon sensor, $500\,\mu\mathrm{m}$ thick, with pixels $50\,\mu\mathrm{m} \times 50\,\mu\mathrm{m}$. We used an ePix camera [9] with several modifications to minimize both scattering and undesired activation (e.g., detector plane

Manuscript received December 9, 2016. SLAC-PUB-16982.

G. Blaj, C. E. Chang, C. J. Kenney, P. Caragiulo, A. Dragone, G. Haller, P. Hansson, C. Hast, R. Herbst, B. Markovic, and T. Smith are with SLAC National Accelerator Laboratory, Menlo Park, CA 94025.

* Corresponding author: blaj@slac.stanford.edu

This material is based upon work supported by the U.S. Department of Energy, Office of Science, Office of High Energy Physics, under Contract DE-AC02-76SF00515.

TABLE I. EPIX100 PIXEL DETECTOR CHARACTERISTICS

	ePix100a
Summary	hybrid pixel detector
Mode of Operation	integrating, 1 gain, fixed
Range	$2.2 \times 10^5\,\mathrm{e}^-$
Noise	$41\,\mathrm{e}^-$
ASIC pixel array size	352×384 pixels
Pixel size	$50\,\mu\mathrm{m} \times 50\,\mu\mathrm{m}$
Typical sensor thickness	$500\,\mu\mathrm{m}$

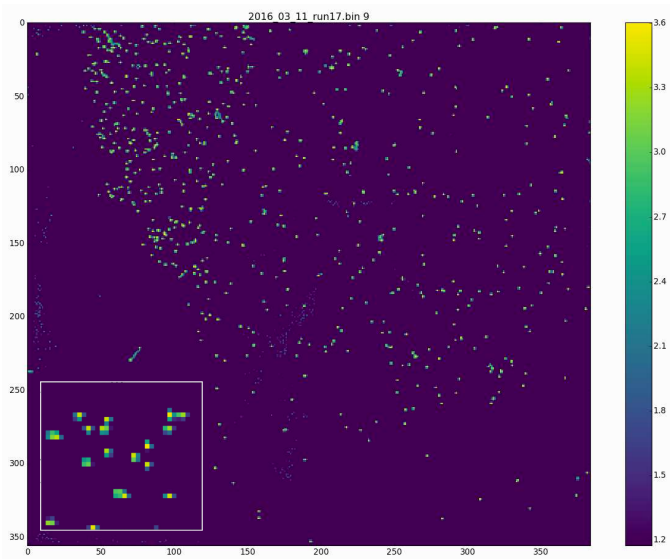

Fig. 2. Typical single frame acquisition with electrons at normal incidence (logarithmic scale). Most electrons share the charge over multiple pixels. Lower left inset shows a close-up of an area with multiple electron hits, some of them overlapping.

rotated by 90° and a minimum of material in the direct beam, especially higher Z material).

For detector characterization experiments we placed the ePix100a camera in the direct electron beam at several incidence angles: normal on the detector plane (90°), at $\sim 45°$, and at $\sim 70°$.

For vertexing measurements, a scattering target (lead, $\sim 10\,\mathrm{mm}$ thick) was mounted $\sim 10\,\mathrm{mm}$ in front of the detector, thus producing diverging showers in addition to the direct electron beam.

B. Track Analysis

At normal incidence, the energy deposited by one electron is often shared between 4 neighboring pixels, allowing reconstruction of the impact point with subpixel resolution. Fig. 2 shows a typical frame with multiple electrons entering the detector at normal incidence. The figure inset illustrates both the charge sharing and pile-up (overlapping of multiple charge clouds).

Each frame was simultaneously fitted for all detected electrons N_{e^-}, modeling the signal induced by electron k entering the detector at coordinates (y_k, x_k) in pixel (i, j) with:

$$I_{ij}(y_k, x_k, E_k, \sigma_k) = \frac{E_k}{2\,\pi\,\sigma_k^2} \int_{i-\frac{1}{2}}^{i+\frac{1}{2}} \mathrm{e}^{-\frac{(y-y_k)^2}{2\sigma_k^2}}\, dy \int_{j-\frac{1}{2}}^{j+\frac{1}{2}} \mathrm{e}^{-\frac{(x-x_k)^2}{2\sigma_k^2}}\, dx \quad (1)$$

and minimizing χ^2 for each frame V_{ij}:

$$\chi^2(y, x, E, \sigma) = \sum_{i=1}^{N_{row}} \sum_{j=1}^{N_{col}} \left(\sum_{k=0}^{N_{e^-}} I_{ij}(y_k, x_k, E_k, \sigma_k) - V_{ij} \right)^2 \quad (2)$$

by fitting the N_{e^-} sets of (x, y, E, σ) corresponding to the N_{e^-} electrons. This allows accurate reconstruction of individual tracks even with up to 3 overlapping tracks while also yielding charge cloud sizes and deposited energies for each individual track.

For relatively thin detectors, the probability density function of measured energies E follows a Landau distribution (a special case of the stable distribution, with $\alpha = 1$ and $\beta = 1$) and can be approximated with the Moyal distribution [10]:

$$p(E) = \frac{1}{\sigma\sqrt{2\,\pi}} \exp\left\{ -\frac{1}{2}\left(\frac{E-\mu}{\sigma} + \mathrm{e}^{-\frac{E-\mu}{\sigma}} \right) \right\} \quad (3)$$

While the Moyal distribution is not a perfect approximation for the Landau distribution, it is often used due to its simplicity [11].

Note that μ and σ are not the expected (mean value) and standard deviation of the distribution, despite some similarities with, e.g., the normal distribution. Using the approximation in Eq. 3, μ corresponds to the most probable energy. We can calculate the mean energy:

$$\mu_E = \int_{-\infty}^{\infty} E\; p(E)\; dE = \mu + \sigma(\gamma + \ln 2) \quad (4)$$

(with $\gamma = 0.577\,215\ldots$ the Euler gamma constant), and the standard deviation:

$$\sigma_E = \int_{-\infty}^{\infty} (E - \mu_E)^2\; p(E)\; dE = \frac{\pi\,\sigma}{\sqrt{2}}. \quad (5)$$

III. RESULTS

A. Electron Beam Imaging

The distribution of charge cloud sizes (σ of 2D Gaussian charge clouds, expressed in $50\,\mu\mathrm{m}$ pixels) is shown in Fig. 3 with a blue line. Note the two peaks at 0.11 and 0.22, corresponding to single pixel events (entire charge collected in a single pixel) and charge sharing events (charge collected in multiple pixels). The red line indicates a two Gaussian peak fit of the distribution.

For position reconstruction with subpixel resolution it is desirable to minimize the probability of single pixel events and maximize the probability of charge sharing events, while keeping the sensor fully depleted. We could achieve this by using a $80\,\mathrm{V}$ to $100\,\mathrm{V}$ sensor bias.

Fig. 4 shows the distribution of subpixel positions ($x - \mathrm{round}(x)$ and $y - \mathrm{round}(y)$ of 2D Gaussian along the x axis,

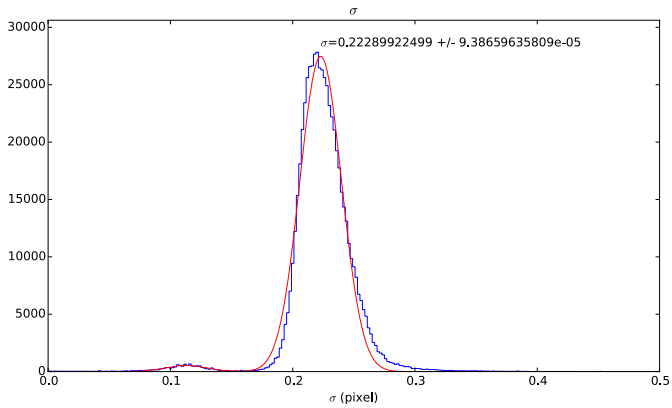

Fig. 3. The distribution of charge cloud sizes is indicated by the blue line. The x axis represents σ of 2D Gaussians, expressed in $50\,\mu\mathrm{m}$ pixel pitch, resulting from fitting with overlapping 2D charge clouds. The distribution of charge cloud sizes shows a bimodal distribution: most tracks share charge over multiple pixels (right, at 0.23 x pixel size) while a small fraction ($\sim 4\,\%$) are single pixel events (left, 0.12 x pixel size). The red line indicates a two Gaussian peak fit of the distribution.

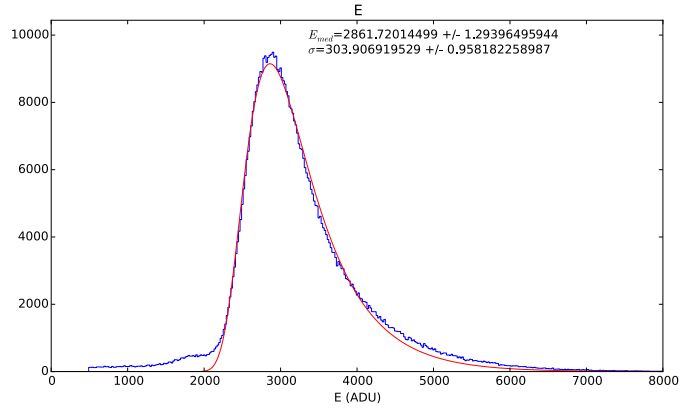

Fig. 5. Blue line indicates the distribution of energies deposited in the sensor (E of 2D Gaussian along the x axis, expressed in detector ADU units) resulting from fitting with overlapping 2D charge clouds. The distribution is consistent with the expected Landau distribution shape (fit indicated by the red line), with parameters $\mu = 2861.7 \pm 1.3$ ADUs and $\sigma = 303.9 \pm 1.0$ ADUs (corresponding to a mean energy of ~ 3248 ADUs and a standard deviation of ~ 675 ADUs for single electron tracks).

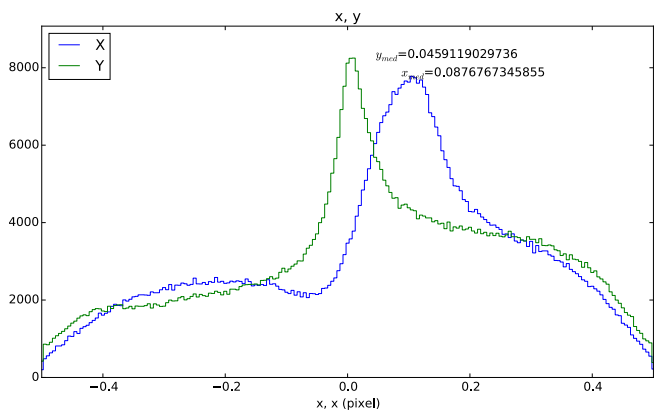

Fig. 4. Distribution of subpixel positions ($x - \mathrm{round}(x)$ and $y - \mathrm{round}(y)$ of 2D Gaussian along the x axis, expressed in detector ADU units) resulting from fitting with overlapping 2D charge clouds indicated by the blue and green lines, respectively. To find the physical subpixel coordinates, this distribution has to be linearized. Also note the asymmetry, due to the beam not being perfectly perpendicular on the detector plane.

expressed in detector ADU units, and $\mathrm{round}(x) = \lfloor x + 1/2 \rfloor$) resulting from fitting with overlapping 2D charge clouds indicated by the blue and green lines, respectively. Note the asymmetry, due to the beam not being perfectly perpendicular on the detector plane.

To find the physical subpixel coordinates, this distribution has to be linearized (by looking up the reverse of the cumulative probability distribution function of the histograms). Once this is done, we obtain a subpixel resolution better than $5\,\mu\mathrm{m}$ (one tenth of the detector pitch, and better near borders between pixels).

Fig. 5 shows the distribution of energies (in detector Analog to Digital Units, ADUs, blue line) together with the corresponding Landau fit (using Eq. 3, red line). The distribution matches the model closely, validating the analysis method. The Landau distribution parameters are $\mu = 2861.7 \pm 1.3$ ADUs and $\sigma = 303.9 \pm 1.0$ ADUs (corresponding to a mean energy of ~ 3248 ADUs and a standard deviation of ~ 675 ADUs). The full range of individual pixels is $16\,384$ ADUs, resulting in a maximum occupancy of about 4 electrons at normal incidence (and increasing for higher angles). (For applications with higher numbers of tracks, the ePix10k detector [12] is a possible alternative, with roughly twice the noise but hundred times the range).

B. 3D Electron Tracking

For describing the 3D track orientation, we use the angles ω and θ to identify the in-plane and out-of-plane angles between the tracks and the detector plane, respectively.

The sensors used in these experiments have a pixel pitch of $50\,\mu\mathrm{m}$ and a thickness of $500\,\mu\mathrm{m}$, resulting in tracks over multiple pixels (e.g., 10 pixels at $45°$, and 28 pixels at $70°$, see Fig. 6. (This effect is also visible at normal incidence, as shown by the asymmetry in Fig. 4).

Fig. 7 shows sample tracks (on logarithmic scale) with the beam incident at $70°$, with an angle θ close to $\pi/2$. Careful investigation reveals a slightly increased line width towards the top of the image, corresponding to the part of the track closer to the front entrance window. This is expected, as the charge deposited near the front of the sensor diffuses more than the charge deposited near the back of the sensor (also illustrated in Fig. 6). We can use this effect to determine for each track which end is near the detector front and which is near the back side, resulting in a unique (non degenerate) 3D track determination.

After extracting the 3D orientation of all tracks, we collected the resulting ω and θ angles in histograms shown in Fig. 8.

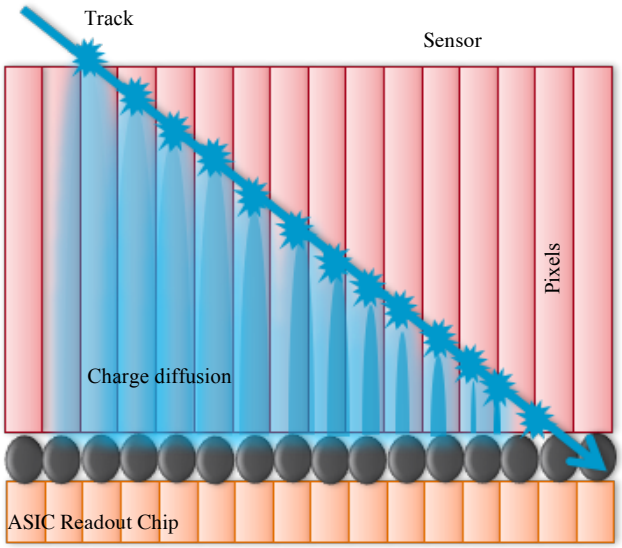

Fig. 6. Electron tracking in pixel detectors: cartoon of section in a pixelated detector with an electron track; ePix100a has a pitch of $50\,\mu\mathrm{m}$ and sensor thickness of $500\,\mu\mathrm{m}$. The out-of-plane angle of incidence can be calculated from the number of pixels in a track and can be refined by fitting an accurate charge cloud model.

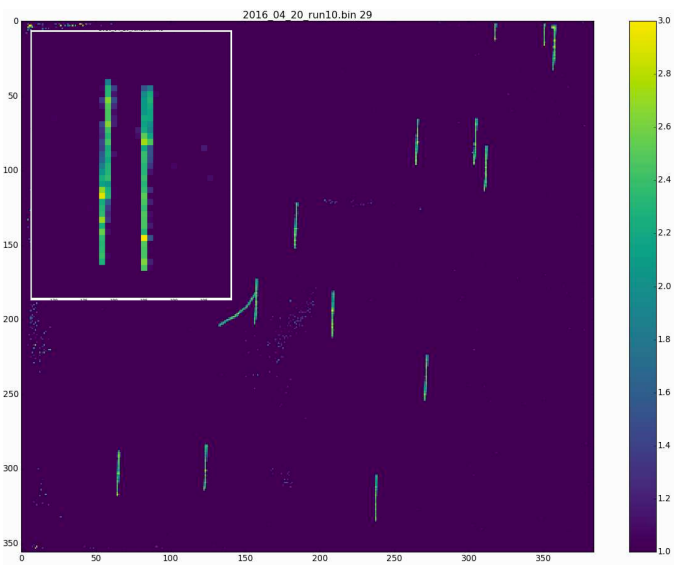

Fig. 7. Typical single frame acquisition with electrons at 70° incidence (logarithmic scale). Occasional delta rays are observed, however, they can be easily identified. Inset (top left) shows selected tracks.

They display a good angular precision: $\omega = 88.03° \pm 0.61°$ and $\theta = 71.12° \pm 0.68°$, better than $\sim 0.7°$ r.m.s. Together with the high subpixel resolution, we obtained the full 3D position and orientation of individual tracks.

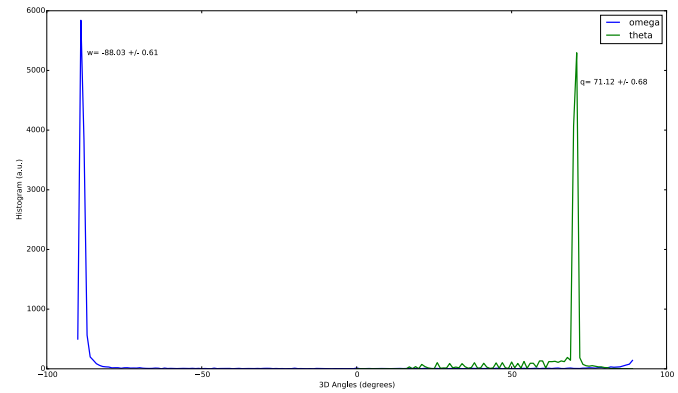

Fig. 8. The histograms of both ω (angle in the detector plane, blue line) and θ (angle outside the plane, green line): $\omega = 88.03° \pm 0.61°$ and $\theta = 71.12° \pm 0.68°$, with an angular precision better tna $\sim 0.7°$ rms.

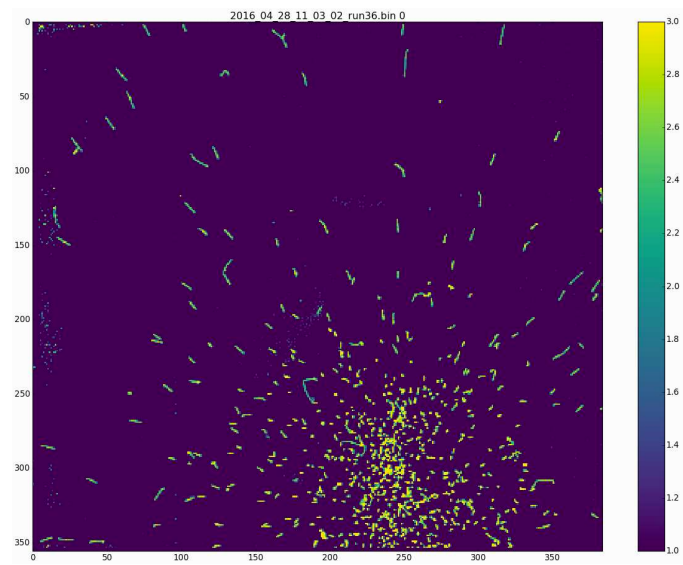

Fig. 9. Typical single frame acquisition with scattering target. Electrons at normal incidence are visible near the lower edge slightly to the right, with particle showers leaving diverging tracks in the other areas.

C. Virtual Vertexing in Single Detector Plane

Using a scattering target ($10\,\mathrm{mm}$ thick lead brick mounted $10\,\mathrm{mm}$ in front of the detector), we were able to collect tracks with scattered electrons diverging from the scatterer, in addition to the parallel direct beam at normal incidence.

Fig. 9 shows a typical single frame acquisition with scattering target. Electrons at normal incidence are visible near the lower edge slightly to the right, with particle showers leaving diverging tracks in the other areas.

After reconstructing the 3D position and orientation of all the tracks, we selected only tracks of scattered electrons (ignoring the direct beam tracks) and projected them onto a 3D volume with $384 \times 352 \times 500$ voxels along the xyz axes and a voxel size of $50\,\mu\mathrm{m} \times 50\,\mu\mathrm{m} \times 50\,\mu\mathrm{m}$. The volume is

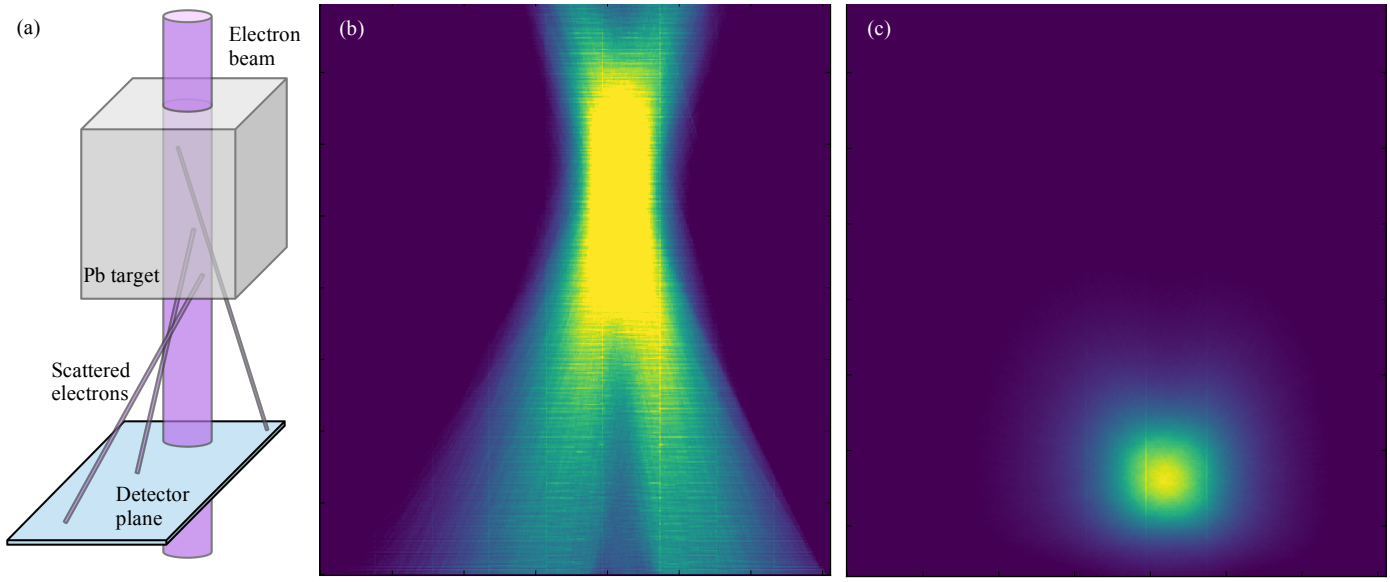

Fig. 10. Individual electron tracks, excluding direct beam tracks, were traced through a 3D volume of $384 \times 352 \times 500$ voxels with one side (z=0) directly above the detector plane and aligned with the detector pixels. (a) shows a reference diagram of the experimental set-up, and (b) shows the projection of the 3D volume onto the xz plane. The origin of most tracks is in the volume corresponding to the intersection of the electron beam with the scattering target (lead brick); (c) shows the projection of the 3D volume onto the xy (detector) plane. While all direct beam tracks were removed from the data set shown here, the scattered electrons unambiguously identify the volume of the intersection between the direct electron beam and the scattering target.

oriented with the xy face corresponding to z=0 just above the sensor face and aligned with the pixel matrix.

In Fig. 10, (a) shows a reference diagram of the experimental set-up, and (b) shows the projection of the 3D volume onto the xz plane. The origin of most tracks is in the volume corresponding to the intersection of the electron beam with the scattering target (lead brick); (c) shows the projection of the 3D volume onto the xy (detector) plane.

While all direct beam tracks were removed from the data set shown here, we can easily identifying the scattering volume (i.e., intersection between the direct electron beam and the scattering target). The tracking and (virtual) vertexing is remarkably accurate for a single pane detector.

IV. Conclusion

ePix100a has a high signal to noise ration (SNR ~ 500 to 1000), exceeding the typical requirements for pixel detectors in particle tracking.

This high SNR results in excellent accuracy: better than $5\,\mu\mathrm{m}$ subpixel resolution and about $0.7\,\mathrm{degree}$ for both the in-plane and out-of-plane angles of the tracks, which are significantly better than expected from the pixel size and detector thickness. Accurate (virtual) vertexing is thus possible with a single ePix100a (low noise) detector plane.

The performance of the virtual vertexing was tested with a scattering target placed at a known position in the electron beam. Reconstructing the vertices and tracing them through a 3D volume yielded results which were consistent with the experimental setup layout, demonstrating the posibility of virtual vertexing in single low-noise detector planes.

Acknowledgment

Use of the Linac Coherent Light Source (LCLS), SLAC National Accelerator Laboratory, is supported by the U.S. Department of Energy, Office of Science, Office of Basic Energy Sciences under Contract No. DE-AC02-76SF00515.

References

[1] A. Nomerotski, "Silicon detectors for tracking and vertexing," *Nuclear Instruments and Methods in Physics Research Section A: Accelerators, Spectrometers, Detectors and Associated Equipment*, vol. 598, pp. 33–40, 2009. [Online]. Available: https://dx.doi.org/doi:10.1016/j.nima.2008.08.020

[2] C. J. Kenney, S. I. Parker, V. Z. Peterson, W. J. Snoeys, J. D. Plummer, and C. H. Aw, "A prototype monolithic pixel detector," *Nuclear Instruments and Methods in Physics Research Section A: Accelerators, Spectrometers, Detectors and Associated Equipment*, vol. 342, no. 1, pp. 59–77, 1994. [Online]. Available: https://dx.doi.org/10.1016/0168-9002(94)91411-7

[3] G. Blaj, P. Caragiulo, G. Carini, S. Carron, A. Dragone, D. Freytag, G. Haller, P. A. Hart, R. Herbst, S. Herrmann, J. Hasi, C. J. Kenney, B. Markovic, K. Nishimura, S. Osier, J. Pines, J. Segal, A. Tomada, and M. Weaver, "Detector development for the Linac Coherent Light Source," *Synchrotron Radiation News*, vol. 27, no. 4, pp. 14–19, 2014. [Online]. Available: https://dx.doi.org/10.1080/08940886.2014.930803

[4] G. Blaj, P. Caragiulo, A. Dragone, G. Haller, J. Hasi, C. J. Kenney, M. Kwiatkowski, B. Markovic, J. Segal, and A. Tomada, "X-ray imaging with ePix100a, a high-speed, high-resolution, low-noise camera," *SPIE Proceedings*, vol. 9968, pp. 99 680J–99 680J–10, June 2016. [Online]. Available: https://dx.doi.org/10.1117/12.2238136

[5] M. Pivi, M. Dunning, C. Hast, T. Fieguth, R. Iverson, J. Jaros, K. Jobe, L. Keller, T. Maruyama, D. Walz *et al.*, "Status of ESTB: a novel beam test facility at SLAC," in *Proceedings of IPAC 2012*. IPAC, 2012.

[6] P. Emma, R. Akre, J. Arthur, R. Bionta, C. Bostedt, J. Bozek, A. Brachmann, P. Bucksbaum, R. Coffee, F.-J. Decker, Y. Ding, D. Dowell, S. Edstrom, A. Fisher, J. Frisch, S. Gilevich, J. Hastings, G. Hays, P. Hering, Z. Huang, R. Iverson, H. Loos, M. Messerschmidt, A. Miahnahri, S. Moeller, H.-D. Nuhn, G. Pile, D. Ratner, J. Rzepiela, D. Schultz, T. Smith, P. Stefan, H. Tompkins, J. Turner, J. Welch, W. White, J. Wu, G. Yocky, and J. Galayda, "First lasing and operation of an ångström-wavelength free-electron laser," *Nature Photonics*, vol. 4, no. 9, pp. 641–647, 2010. [Online]. Available: https://dx.doi.org/10.1038/nphoton.2010.176

[7] B. Markovic, A. Dragone, P. Caragiulo, R. Herbst, K. Nishimura, B. Reese, S. Herrmann, P. A. Hart, G. Blaj, J. Segal, A. Tomada, J. Hasi, G. Carini, C. J. Kenney, and G. Haller, "Design and characterization of the ePix100a prototype: a low noise integrating pixel ASIC for LCLS detectors," in *2014 IEEE Nuclear Science Symposium and Medical Imaging Conference (NSS/MIC)*. IEEE, Nov 2014, pp. 1–3. [Online]. Available: https://dx.doi.org/10.1109/NSSMIC.2014.7431230

[8] A. Dragone, P. Caragiulo, B. Markovic, R. Herbst, K. Nishimura, B. Reese, S. Herrmann, P. A. Hart, G. Blaj, J. Segal, A. Tomada, J. Hasi, G. Carini, C. J. Kenney, and G. Haller, "ePix: a class of front-end ASICs for second generation LCLS integrating hybrid pixel detectors," in *2013 IEEE Nuclear Science Symposium and Medical Imaging Conference (2013 NSS/MIC)*. IEEE, Oct 2013, pp. 1–5. [Online]. Available: https://dx.doi.org/10.1109/NSSMIC.2013.6829505

[9] K. Nishimura, G. Blaj, P. Caragiulo, G. Carini, A. Dragone, G. Haller, P. Hart, J. Hasi, R. Herbst, S. Herrmann, C. J. Kenney, M. Kwiatkowski, B. Markovic, S. Osier, J. Pines, B. Reese, J. Segal, A. Tomada, and M. Weaver, "Design and performance of the ePix camera system," *AIP Conference Proceedings*, vol. 1741, no. 1, p. 040047, 2016. [Online]. Available: https://dx.doi.org/10.1063/1.4952919

[10] J. Moyal, "XXX. Theory of ionization fluctuations," *The London, Edinburgh, and Dublin Philosophical Magazine and Journal of Science*, vol. 46, no. 374, pp. 263–280, 1955. [Online]. Available: https://dx.doi.org/10.1080/14786440308521076

[11] M. Marucho, C. A. Garcia Canal, and H. Fanchiotti, "The Landau distribution for charged particles traversing thin films," *International Journal of Modern Physics C*, vol. 17, no. 10, pp. 1461–1476, 2006. [Online]. Available: https://dx.doi.org/10.1142/S0129183106009928

[12] P. Caragiulo, A. Dragone, B. Markovic, R. Herbst, K. Nishimura, B. Reese, S. Herrmann, P. Hart, G. Blaj, J. Segal, A. Tomada, J. Hasi, G. Carini, C. J. Kenney, and G. Haller, "Design and characterization of the ePix10k prototype: A high dynamic range integrating pixel ASIC for LCLS detectors," in *2014 IEEE Nuclear Science Symposium and Medical Imaging Conference (NSS/MIC)*. IEEE, Nov 2014, pp. 1–3. [Online]. Available: https://dx.doi.org/10.1109/NSSMIC.2014.7431049